

Spin-Orbit Coupling Effect on the Seebeck Coefficient in Dirac Electron Systems in α -(BETS) $_2$ I $_3$

Yoshikazu Suzumura,^{1,*} Takao Tsumuraya,^{2,†} and Masao Ogata^{3,‡}

¹*Department of Physics, Nagoya University, Nagoya 464-8602, Japan*

²*Magnesium Research Center, Kumamoto University, Kumamoto 860-8555, Japan*

³*Department of Physics, University of Tokyo, Bunkyo, Tokyo 113-0033,*

Japan and National Institute of Advanced Industrial Science and Technology (AIST), Tsukuba, Ibaraki 305-8568, Japan

(Dated: September 10, 2025)

Seebeck coefficient, $S = L_{12}/(TL_{11})$, which is proportional to a ratio of the thermoelectric conductivity L_{12} to the electric conductivity L_{11} with T being temperature is examined for two-dimensional Dirac electrons in a three-quarter filled organic conductor, α -(BETS) $_2$ I $_3$, [BETS = BEDT-TSeF = bis(ethylenedithio)tetraselenafulvalene] at ambient pressure. Using a tight-binding (TB) model obtained by first-principles relativistic density-functional theory method [Eur. Phys. J. B 94, 17 (2021)], we calculate S in the presence of the impurity and electron-phonon (e-p) scatterings. It is shown that $S_x < 0$ and $S_y > 0$ at high temperatures, where S_x (S_y) denotes S perpendicular (parallel) to the molecular stacking axis. There is a sign change of S_y with increasing T . It is found that, at low temperatures the absolute value of S is enhanced by the spin-orbit coupling. The Seebeck coefficient is examined by dividing into components of the conduction and valence bands to find that the electron and hole contributions compete each other. Such T dependence of S is clarified using the spectral conductivity, which determines L_{12} and L_{11} .

I. INTRODUCTION

Two-dimensional massless Dirac fermions (MDF) with a linear spectrum around a Dirac point have been studied extensively.¹ Among them, a bulk material has been found in an organic conductor,² α -(BEDT-TTF) $_2$ I $_3$, where BEDT-TTF = bis(ethylenedithio)tetrathiafulvalene.³ This material exhibits a zero-gap state (ZGS) in the energy band due to the Dirac cone^{4,5}, which is calculated using a tight-binding (TB) model with transfer energies estimated from the extended Hückel method.^{6,7} The transport properties of such a system is affected by the density of states (DOS), which reduces linearly to zero at the Fermi energy.⁵ A first-principles calculation based on density functional theory (DFT) confirmed the existence of MDF in α -(BEDT-TTF) $_2$ I $_3$ at ambient pressure.⁸ Under hydrostatic pressure, a DFT band structure⁹ has been calculated using the crystal structure determined by x-ray diffraction measurements at 1.76 GPa.⁷ Despite these investigations, the impact of pressure on the transfer energies calculated through first-principles methods has not been explored. Thus, a new model has been presented by deriving an *ab initio* TB model¹⁰ with the experimentally obtained crystal structure.⁷

Characteristic properties of the MDF appear in the temperature (T) dependence of various physical quantities. The T -linear behavior of the magnetic susceptibility^{11,12} and the sign change of the Hall coefficient,¹³ have been well understood by theories using the four-band model¹⁴ and the two-band model^{15,16}, respectively. However, almost T -independent conductivity^{17–21} cannot be understood by a model with only impurity scattering.²² If we consider the effect of electron-phonon (e-p) interaction, a nearly-constant conductivity can be understood using a simple two-band model of the Dirac cone without

tilting.²³ Noting that the energy band in the actual organic conductor deviates from the linear spectrum,²⁴ the conductivity has been calculated using the TB model of α -(BEDT-TTF) $_2$ I $_3$ with the e-p interaction.²⁵

In organic conductors, Dirac electrons are also expected for α -(BETS) $_2$ I $_3$ [BETS = BETS-TSeF = bis(ethylenedithio)tetraselenafulvalene], since the almost constant resistivity has been observed at high temperatures.²⁶ The gradual increase of resistivity at low temperatures in α -(BETS) $_2$ I $_3$ shows an insulating behavior but no symmetry breaking in contrast to the charge ordering of α -(BEDT-TTF) $_2$ I $_3$.^{27–29} Noting a spin-orbit interaction (SOI) in organic conductors,³⁰ an explicit TB model with SOI has been derived for α -(BEDT-TTF) $_2$ I $_3$, where the transfer energies are complex and provides the Berry curvature of spin subbands.³¹ As for α -(BETS) $_2$ I $_3$, the band calculation based on the extended Hückel method,⁷ gives the Dirac point but the metallic state due to the over-tilted Dirac cone. Thus, the first-principles DFT calculation was performed to show the Dirac electron with a small gap ~ 2 meV due to the spin-orbit coupling (SOC) and an effective model with transfer energies was derived.³² Because of the SOC-induced gap, spin Hall conductivity and anomalous spin conductivity under a magnetic field are theoretically expected.³³ Using such a TB model with transfer energies being complex and the electron-phonon (e-p) interaction, it was shown that the conductivity at high temperatures is almost constant due to the increase of the scattering by phonon.³⁴ At low temperatures, the increase of resistivity was examined by introducing the on-site Coulomb interaction,³⁵ which is treated by Hartree approximation with the mean field resulting in a second order phase transition (at $T_c \sim 0.003$ eV) to a state of a spin-ordered massive Dirac electron (SMD) with a gap. It is pointed out that such a gap competes with that induced by SOI.

It is of interest to verify experimentally such a magnetic ordered state.³⁶ Further, using *ab initio* and 2D extended Hubbard model treated within Hartree-Fock approximation,³⁷ the metal-insulator crossover at ~ 50 K followed by the ordered states of a quantum spin Hall insulator was shown, where the SOI enhances the resistivity at low temperatures.

In addition to the conductivity, there are several studies on the Seebeck coefficient of organic conductors. The formula of the Seebeck effects has been established using a linear response theory.^{38–41} For α -(BEDT-TTF)₂I₃, the coefficient has been observed experimentally under hydrostatic pressure,^{42,43} which is measured along the x -direction (perpendicular to the molecular stacking axis)⁴². The calculation of the Seebeck coefficient S_ν was performed along the y -direction,⁴⁴ and along the x -direction,⁴⁵ (i.e., the same direction as that in an experiment). With decreasing temperature, the former at ambient pressure shows the decrease of S_y by taking account of the correlation, while the latter under a uniaxial pressure shows the sign change and a minimum at low temperatures. Although the case of uniaxial pressure shows $S_x > 0$ at high temperatures and exhibits qualitatively the same T dependence as that of the experiment, a problem still remains for the case of hydrostatic pressure. A model calculation using the transfer energies obtained by the extended Hückel method⁷ with a previous first-principles calculation at ambient pressure⁸ gives a negative Seebeck coefficient ($S_x < 0$),⁴⁵ whereas experimental results show a positive Seebeck coefficient at finite temperatures.^{42,43} Then, using a TB model obtained from an *ab initio* calculation with the experimentally obtained crystal structure at 1.76 GPa,⁷ it was shown that the Seebeck coefficients in α -(BEDT-TTF)₂I₃ under hydrostatic pressure are positive in both x - and y -directions¹⁰ indicating the hole-like behavior. For understanding a competition between the conduction and valence bands, a method at low temperatures has been proposed, where the sign of S is determined by that of the energy derivative of the spectral conductivity $\sigma_\nu(\epsilon, T)$ with respect to ϵ at a chemical potential.⁴⁵ It was recently reported⁴⁶ that the Seebeck coefficient in α -(BETS)₂I₃ shows a noticeable difference from that in α -(BEDT-TTF)₂I₃, i.e., S_x is negative in contrast to $S_x > 0$ in α -(BEDT-TTF)₂I₃ and S_y changes sign from negative to positive as the temperature increases. It is important to clarify the origin of these differences between α -(BETS)₂I₃ and α -(BEDT-TTF)₂I₃.

In this paper, we study theoretically the Seebeck coefficient of α -(BETS)₂I₃ using a TB model with transfer energies, which are derived from the first principles relativistic DFT calculation.^{32,34} The present paper is organized as follows. In Sect. 2, a formulation for α -(BETS)₂I₃ is given, where a TB model consists of transfer energies with both real and imaginary parts. Electronic states of the TB model are shown using the conduction and valence energy bands around the Dirac point and the density of states. In Sect. 3, the Seebeck coef-

ficient S is calculated by adding the impurity and e-p scatterings. The T dependence of S for both x and y directions is shown and analyzed in terms of the spectral conductivity with velocities. Section 4 is devoted to summary and discussion.

II. MODEL AND ELECTRONIC STATES

A. Model Hamiltonian

We consider a two-dimensional Dirac electron system, which is given by³⁴

$$H = H_0 + H_p + H_{e-p} + H_{\text{imp}}. \quad (1)$$

Here, H_0 describes a TB model of the organic conductor, α -(BETS)₂I₃, consisting of four molecules per unit cell (Fig. 1). The second term denotes the harmonic phonon given by $H_p = \sum_{\mathbf{q}} \omega_{\mathbf{q}} b_{\mathbf{q}}^\dagger b_{\mathbf{q}}$ with $\omega_{\mathbf{q}} = v_s |\mathbf{q}|$ and $\hbar = 1$. The third term is the electron-phonon (e-p) interaction with a coupling constant $g_{\mathbf{q}}$,

$$H_{e-p} = \sum_{s=\pm} \sum_{\mathbf{k}, \gamma} \sum_{\mathbf{q}} g_{\mathbf{q}} c_{\gamma s}(\mathbf{k} + \mathbf{q})^\dagger c_{\gamma s}(\mathbf{k}) (b_{\mathbf{q}} + b_{-\mathbf{q}}^\dagger). \quad (2)$$

$c_{\gamma s}(\mathbf{k}) = \sum_{\alpha} d_{\alpha \gamma} a_{\alpha s}(\mathbf{k})$ with spin s , which is obtained by diagonalizing H_0 as shown later. The e-p scattering is considered within the same band (i.e., intraband). The last term of Eq. (1), H_{imp} , denotes a normal impurity scattering.

The TB model, H_0 , is expressed as

$$H_0 = \sum_{i,j=1}^N \sum_{\alpha, \beta=1}^4 \sum_{s, s'=\pm} t_{ij; \alpha s, \beta s'} a_{i \alpha s}^\dagger a_{j \beta s'}, \quad (3)$$

where $a_{i \alpha s}^\dagger$ denotes a creation operator of an electron at the molecule α [$= A(1), A'(2), B(3),$ and $C(4)$] in the unit cell with the i -th lattice site. $s = +$ and $s = -$ denote \uparrow and \downarrow spins, respectively. N is the total number of square lattice sites and $t_{ij; \alpha s, \beta s'}$ are the transfer energies for the nearest neighbor (NN) and next-nearest neighbor (NNN) sites.³² H_0 is rewritten using a Fourier transform of the operator $a_{j, \alpha, s}$, which is given by $a_{j, \alpha, s} = 1/N^{1/2} \sum_{\mathbf{k}} a_{\alpha s}(\mathbf{k}) \exp[i\mathbf{k} \cdot \mathbf{r}_j]$. The wave vector $\mathbf{k} = (k_x, k_y)$ is taken within \mathbf{G} , which denotes a reciprocal lattice vector of the square lattice. The quantity $\mathbf{G}/2$ corresponds to the vector of the time-reversal invariant momentum (TRIM). Thus, H_0 is rewritten as

$$H_0 = \sum_{\mathbf{k}} \sum_{s, s'} \sum_{\alpha, \beta} h_{\alpha \beta; ss'}(\mathbf{k}) a_{\alpha s}^\dagger(\mathbf{k}) a_{\beta s'}(\mathbf{k}). \quad (4a)$$

The transfer energy $h_{\alpha \beta; ss'}(\mathbf{k})$ is expressed as

$$h_{\alpha \beta; ss'}(\mathbf{k}) = \sum_{j(\neq i)} t_{ij; \alpha s, \beta s'} \exp[-i\mathbf{k} \cdot (\mathbf{r}_i - \mathbf{r}_j)], \quad (4b)$$

where site potentials are added as shown in Appendix A. In Eqs. (4a) and (4b), the SOC is included due to the d electrons in Se atom.

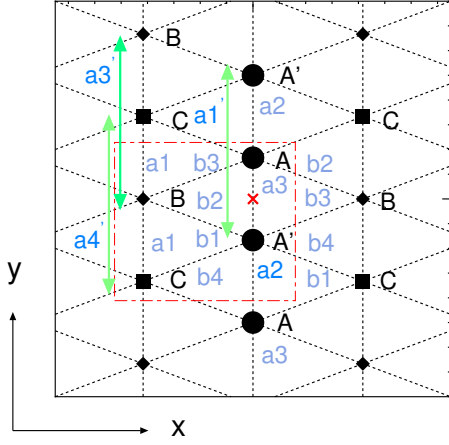


Figure 1. (Color online) Crystal structure of α -(BETS) $_2$ I $_3$. There are four molecules A, A', B and C in a unit cell (dot-dash line), which forms a square lattice. The transfer energies of the same spin (opposite spin) are shown in Table I (Table II); the energies for the nearest neighbor (NN) sites are given by a_1, \dots, b_4 . Those for the next-nearest neighbor (NNN) sites with the same molecules are given by a_1', a_3' , and a_4' along the k_y direction and s_1, \dots, s_4 (not shown here) along the k_x direction, respectively. Those for NNN sites with different kinds of molecules are given by c_1, \dots, c_4 and d_0, \dots, d_3 , which are not shown here but we refer our previous paper³². The cross denotes an inversion center between A and A'. x (y) denotes a coordinate perpendicular to (along) a molecular stacking direction.

B. Transfer energies of TB model

The transfer energy $t_{ij;\alpha s, \beta s'}$ in Eq.(3) is derived from first-principles DFT calculations.³² It is given by

$$t_{\alpha\beta;ss'}(\mathbf{R}) = \langle \phi_{\alpha s,0} | H_k | \phi_{\beta s',\mathbf{R}} \rangle, \quad (5)$$

where H_k is the one-body part of the *ab initio* Hamiltonian for α -(BETS) $_2$ I $_3$.⁸ $\phi_{\alpha s,\mathbf{R}}$ denotes the maximally-localized Wannier function (MLWF) spread over the BETS molecule, with αs representing distinct MLWFs. \mathbf{R} indicates the location of the j -th unit cell relative to the i -th unit cell. The crystal structure is based on the experimental structure at 30 K and ambient pressure²⁹, with hydrogen positions optimized using first-principles methods.

As shown in Eq.(5), $t_{ij;\alpha s, \beta s'}$ depends solely on the relative positions of the i -th and j -th sites. Using Bloch functions obtained from DFT calculations^{47,48}, we constructed the MLWFs with the `wannier90` code^{49,50}. Each MLWF is centered at the midpoint of the central C=C bonds in the BETS molecule. To construct MLWFs, we selected eight bands near the Fermi level (four bands consisting of HOMO of BETS molecule with up and down spins). The DFT band structure including SOC is calculated using full-relativistic pseudopotentials with plane-wave basis sets in Quantum ESPRESSO.^{51–53} For the exchange-correlation functional, we used

the Perdew-Burke-Ernzerhof (PBE) generalized gradient approximation (GGA)⁵⁴. The full-relativistic pseudopotentials were generated using atomic code (version 6.3)⁵⁵ with a pseudization algorithm proposed by Troullier and Martins⁵⁶. The valence configurations were $(1s)^1$ for H, $(2s)^2(2p)^2$ for C, $(3s)^2(3p)^4$ for S, $(4s)^2(4p)^4(4d)^{10}$ for Se, and $(5s)^2(5p)^5(4d)^{10}$ for I atoms. The cutoff energies for plane waves and charge densities were 48 and 488 Ry, respectively. For self-consistent loops, we employed a $4 \times 4 \times 2$ uniform \mathbf{k} -point mesh with Gaussian smearing. The computational details are provided in our previous work.^{32,34}

In Tables I and II, the transfer energies w_h obtained from Eq. (5) are shown, where $w_h(s = s')$ and $w_h(s = -s')$ correspond to the same spin and opposite spin, respectively. In Table I, the nearest neighbor (NN) interactions are labeled a_1, \dots, b_4 , while the next-nearest neighbor (NNN) interactions are labeled a_1', \dots, a_4' , c_1, \dots, c_4 , d_0, \dots, d_3 and s_1, \dots, s_4 , respectively.^{32,34} The quantities V_α represent the on-site potential energies. Since the origin of the energy is arbitrary, we measure the on-site potentials V_B and V_C relative to those of A and A' (Appendix A). All energies are expressed in eV.

C. Electronic states

There are three kinds of SOC, which act on the the same spins ($s = s'$) and the opposite spins ($s = -s'$) with two components of spin freedom, respectively. The former case (the latter case) is defined by SOC I (SOC II) and is treated by a spin decoupled 4×4 matrix Hamiltonian (by a 8×8 matrix Hamiltonian coupled by up and down spins). Further, SOC III is defined as the case of only the real part of SOC I, which also includes SOC.

The band energy of the a TB model $H_0(\mathbf{k})$ is obtained by

$$\sum_{\beta, s'} h_{\alpha\beta;ss'}(\mathbf{k}) d_{\beta s'\gamma}(\mathbf{k}) = E_\gamma(\mathbf{k}) d_{\alpha s\gamma}(\mathbf{k}), \quad (6)$$

where $h_{\alpha\beta;ss'}(\mathbf{k})$ with the same spin is shown in Appendix A. $E_\gamma(\mathbf{k})$ with $\gamma = 1, \dots, 4$ for the spin decoupled Hamiltonian (with $\gamma = 1, \dots, 8$ for the spin coupled Hamiltonian) denotes the band energy in the descending order. The Dirac point (\mathbf{k}_D) is obtained from a minimum of $E_c(\mathbf{k}) - E_v(\mathbf{k}) (> 0)$, where $E_c(\mathbf{k})$ and $E_v(\mathbf{k})$ are the conduction and valence bands above and below a chemical potential, respectively.

From the three-quarter-filled condition, the chemical potential μ is calculated by

$$\frac{1}{N(2N)} \sum_{\mathbf{k}} \sum_{\gamma=1}^{4(8)} f(E_\gamma(\mathbf{k}) - \mu) = 3, \quad (7)$$

where $f(\epsilon) = 1/(\exp[\epsilon/k_B T] + 1)$ with T being temperature and a Boltzmann constant taken as $k_B = 1$. Thus,

$E_1(\mathbf{k})$ and $E_2(\mathbf{k})$ for the 4×4 matrix ($E_2(\mathbf{k})$ and $E_3(\mathbf{k})$ for the 8×8 matrix) give the conduction and valence bands, respectively. The density of states (DOS) per spin is calculated from

$$D(\omega) = \frac{1}{N(2N)} \sum_{\mathbf{k}} \sum_{\gamma=1}^{4(8)} \delta(\omega - E_{\gamma}(\mathbf{k})). \quad (8)$$

In Fig. 2, DOS is shown as a function of $\omega - \mu_0$ with μ_0 being μ at $T = 0$. The solid line (SOC I) shows DOS for the same spin ($s = s'$) with both $\text{Re}(w_h(s = s'))$ and $\text{Im}(w_h(s = s'))$, while the dot line (SOC III) denotes DOS only for $\text{Re}(w_h(s = s'))$. The gap on the Dirac point is found as 2.1×10^{-3} for SOC I (solid) but zero for SOC II (dot dash) and SOC III (dot). Thus, the former transfer energy gives rise to the effect of SOC on the transport. The dot dash line (SOC II) shows DOS in the presence of both the same and opposite spins ($s = s'$ and $s = -s'$). For $\omega - \mu_0 \simeq -0.01$, DOS of SOC I and SOC III shows a single peak but DOS of SOC II

Table I. Effective transfer energies $w_h(s = s')$ of the same spin and site-potential energies for α -(BETS) $_2$ I $_3$. ΔV_B and ΔV_C are site-potential energies of B and C molecular sites relative to A (and A') site, respectively. The definitions are shown in Eq. (5) and Appendix A. $t_{\alpha s, \beta, s'} \rightarrow w_h(s = s')$ includes SOC and are labeled $h = a1, \dots, s4$. Note that $\text{Im}(w_h(s = \pm s'))$ is replaced by $\text{sgn}(s)\text{Im}(w_h(s = \pm s'))$.

$w_h(s = s')$	$\text{Re}(w_h)$	$\text{Im}(w_h)$
$a1$	0.0053	0.00130
$a2$	-0.0201	0
$a3$	0.0463	0
$b1$	0.1389	0.00674
$b2$	0.1583	0.00731
$b3$	0.0649	0.00203
$b4$	0.0190	-0.00120
$a1'$	0.0135	0
$a3'$	0.0042	0
$a4'$	0.0217	0
$c1$	-0.0024	-0.00056
$c2$	0.0063	-0.00010
$c3$	-0.0036	-0.00040
$c4$	0.0013	0.00027
$d0$	-0.0009	0
$d1$	0.0104	0
$d2$	0.0042	-0.00009
$d3$	0.0059	-0.00003
$s1$	-0.0016	-0.00017
$s3$	-0.0014	0
$s4$	0.0023	0
ΔV_B	-0.0047	
ΔV_C	-0.0092	

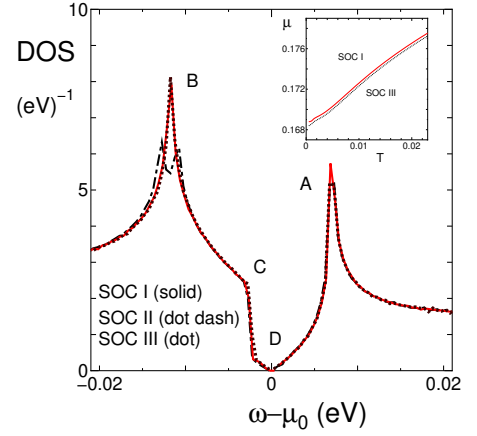


Figure 2. (Color online) DOS per spin as a function of $\omega - \mu_0$, where $\mu_0 = 0.1687$ denotes μ at $T = 0$. The solid line (SOC I) shows DOS with the same spin ($s = s'$), while the dot line (SOC III) denotes DOS only with $\text{Re}(w_h(s = s'))$. The dash dot line (SOC II) shows DOS in the presence of SOC with both the same and opposite spins ($s = s'$ and $s = -s'$). The energy at the Dirac point is shown by D and those of the van Hove singularity are shown by A and B, which are explained later. The inset denotes μ as a function of T .

shows a double peak due to the splitting by the coupling between the opposite spins. There is an asymmetry of DOS around $\omega = \mu_0$. DOS for the conduction band ($\omega > \mu_0$) is smaller than that for the valence band ($\omega < \mu_0$) because of the presence of the shoulder C. Thus, μ at finite temperatures becomes larger than μ_0 . The inset in Fig. 2 shows the T dependence of the chemical potential μ , where μ for SOC I is slightly larger than that for SOC III. With increasing T , μ increases monotonously and we

Table II. Effective transfer energies $w_h(s = -s')$ of opposite spin for α -(BETS) $_2$ I $_3$. Quantities $w_h(s = -s')$, which include SOC and are labeled $h = b1_{so1}, \dots, c4_{so2}$,³², are estimated by averaging two components of spin freedom.

$w_h(s = -s')$	$\text{Re}(w_h)$	$\text{Im}(w_h)$
$b1_{so1}$	-0.0020	0.00077
$b1_{so2}$	0.0020	-0.00077
$b2_{so1}$	-0.0019	-0.00017
$b2_{so2}$	0.0019	0.00017
$b4_{so1}$	0.0008	-0.00097
$b4_{so2}$	-0.0008	0.00097
$c1_{so1}$	0.0007	-0.00033
$c1_{so2}$	-0.0007	0.00033
$c2_{so1}$	0.0003	0.00022
$c2_{so2}$	-0.0003	-0.00022
$c3_{so1}$	0.0006	0.00018
$c3_{so2}$	-0.0006	-0.00018
$c4_{so1}$	0.0001	-0.00008
$c4_{so2}$	-0.0001	0.00008

find that approximately the relation $\mu(T) - \mu_0 \sim 0.4T$ holds.

Hereafter, we examine the case of SOC with the same spin (intra SOC), i.e., the 4×4 matrix Hamiltonian. Using the TB model with transfer energies given by Table I, we examine energy bands obtained from Eq. (6). Figure 3(a) shows conduction and valence bands given by $E_1(\mathbf{k})$ (upper band) and $E_2(\mathbf{k})$ (lower one). There is a Dirac point \mathbf{k}_D , where a gap corresponding to a minimum of $E_2(\mathbf{k}) - E_1(\mathbf{k})$ is found at $\mathbf{k} = \mathbf{k}_D$. Two Dirac points exist at \mathbf{k}_D and $-\mathbf{k}_D$ with $\mathbf{k}_D = -(0.729, -0.577)\pi$ in the 2nd and forth quadrants, respectively on the $k_x - k_y$ plane. [We have put the length of the unit cell is equal to 1.] Figure 3(b) shows the magnified scale of the conduction and valence bands $E_1(\mathbf{k})$ and $E_2(\mathbf{k})$ around \mathbf{k}_D as a function of $\delta\mathbf{k} = \mathbf{k} - \mathbf{k}_D$. They are described by the Dirac cone, which is tilted almost along the k_x axis. Note that the gap ($\simeq 0.002$) at \mathbf{k}_D comes from the SOC, which exists in transfer energies (Table I). Figure 3(c) shows contour plots of $E_1(\mathbf{k}) - E_2(\mathbf{k})$ being a difference between the conduction and valence bands. The contour is similar but deviates from the ellipsoid with the minor axis being close to the k_x axis. The ellipsoid suggests an anisotropy of the Dirac cone leading to the relation, $v_x > v_y$ for the velocity and $\sigma_x > \sigma_y$ for the electric conductivity. A deviation from the ellipsoid results in the Seebeck coefficient.

Figure 3(d) shows contour plots of conduction band $E_1(\mathbf{k})$ near the M' point $(k_x, k_y) = (\pi, -\pi)$. The Dirac points are located at $(k_x/\pi - 1, k_y/\pi + 1) = \pm(-0.271, 0.423)$. The pinch point indicates the saddle point at M', which gives a van Hove singularity at A in Fig. 2. Figure 3(e) shows contour plots of valence band $E_2(\mathbf{k})$ near the Y point $(k_x, k_y) = (0, -\pi)$. The Dirac points are located at $(k_x/\pi, k_y/\pi + 1) = \pm(0.729, 0.423)$. There is a local maximum at the Y point corresponding to the shoulder of C in Fig. 2. There are two saddle points at $(k_x/\pi, k_y/\pi + 1) \simeq \pm(0.40, 0.40)$, which are represented by two pinch points. They give a van Hove singularity at B in Fig. 2.

III. SEEBECK EFFECTS

Using the linear response theory,^{38,39} the electric current density $\mathbf{j} = (j_x, j_y)$ is obtained from the electric field $\mathbf{E} = (E_x, E_y)$ and the temperature gradient ∇T as

$$j_\nu = L_{11}^\nu E_\nu - L_{12}^\nu \nabla_\nu T / T, \quad \text{for } \nu = x, y. \quad (9)$$

The coefficients L_{11}^ν and L_{12}^ν denote the electric conductivity and the thermoelectric conductivity, which are re-

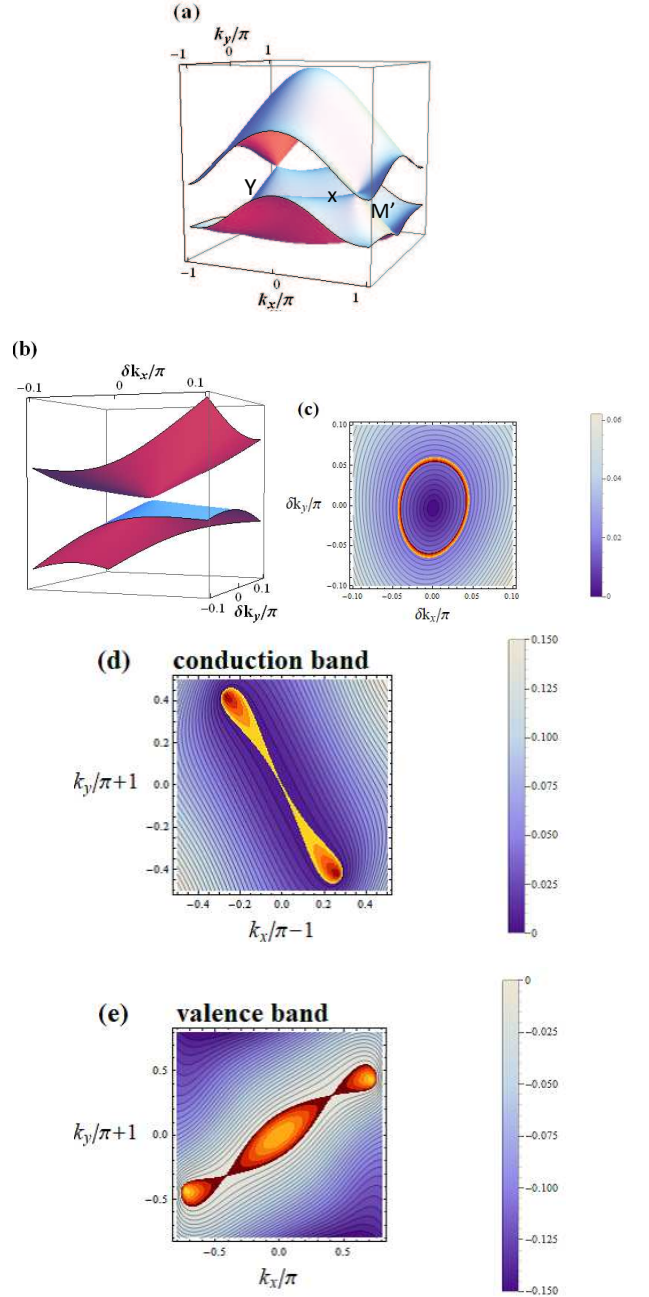


Figure 3. (Color online) (a) Two bands, conduction and valence bands, given by $E_1(\mathbf{k})$ (upper band) and $E_2(\mathbf{k})$ (lower band), which contact at a Dirac point. TRIM's Y and M' denote $(k_x, k_y)/\pi = (0, 1)$ and $(1, -1)$ respectively. A cross x in $E_2(\mathbf{k})$ shows a saddle point on a line connecting Y and the Dirac point. (b) Magnified two bands $E_1(\mathbf{k})$ and $E_2(\mathbf{k})$ showing a tilted Dirac cone around the Dirac point \mathbf{k}_D , where $\delta\mathbf{k} = \mathbf{k} - \mathbf{k}_D$ and $\mathbf{k}_D = -(0.729, -0.577)\pi$. (c) Contour plots of $E_1(\mathbf{k}) - E_2(\mathbf{k})$ on the plane of $\delta\mathbf{k}$, where the red line corresponds to $E_1(\mathbf{k}) - E_2(\mathbf{k}) = 0.02$. (d) Contour plots of conduction band $E_1(\mathbf{k})$ near the M' point $(k_x, k_y) = (\pi, -\pi)$. The yellow to red contours show the region with $0 \leq E_1 - \mu_0 < 0.0074$. The Dirac points are located at $(k_x/\pi - 1, k_y/\pi + 1) = \pm(-0.271, 0.423)$, and the pinch point indicates the saddle point at M'. (e) Contour plots of valence band $E_2(\mathbf{k})$ near the Y point $(k_x, k_y) = (0, -\pi)$. The yellow to red contours show the region with $-0.014 \leq E_2 - \mu_0 \leq 0$. The Dirac points are located at $(k_x/\pi, k_y/\pi + 1) = \pm(0.729, 0.423)$. The energy at Y point has a maximum and there are two saddle points, which are represented by two pinch points.

spectively written as,^{40,41}

$$L_{11}^\nu = \sigma_\nu(T) = \int_{-\infty}^{\infty} d\epsilon \left(-\frac{\partial f(\epsilon - \mu)}{\partial \epsilon} \right) \times \sigma_\nu(\epsilon, T), \quad (10)$$

$$L_{12}^\nu = \frac{-1}{e} \int_{-\infty}^{\infty} d\epsilon \left(-\frac{\partial f(\epsilon - \mu)}{\partial \epsilon} \right) \times (\epsilon - \mu) \sigma_\nu(\epsilon, T). \quad (11)$$

The electric conductivity per spin is given by $\sigma_\nu(T)$. In Eqs. (10) and (11), $\sigma_\nu(\epsilon, T)$ denotes the spectral conductivity, which is expressed in terms of the conduction band ($\gamma = 1$) and valence band ($\gamma = 2$)⁴⁵

$$\sigma_\nu(\epsilon, T) = \sum_{\gamma, \gamma'=1}^2 \sigma_\nu^{\gamma\gamma'}(\epsilon, T), \quad (12)$$

where the component is expressed as

$$\begin{aligned} \sigma_\nu^{\gamma\gamma'}(\epsilon, T) &= \frac{e^2}{\pi \hbar N} \sum_{\mathbf{k}} v_{\gamma\gamma'}^\nu(\mathbf{k})^* v_{\gamma'\gamma}^\nu(\mathbf{k}) \\ &\times \frac{\Gamma_\gamma}{(\epsilon - E_\gamma(\mathbf{k}))^2 + \Gamma_\gamma^2} \cdot \frac{\Gamma_{\gamma'}}{(\epsilon - E_{\gamma'}(\mathbf{k}))^2 + \Gamma_{\gamma'}^2}, \end{aligned} \quad (13)$$

with $v_{\gamma\gamma'}^\nu(\mathbf{k}) = \sum_{\alpha\beta} d_{\alpha\gamma}(\mathbf{k})^* (\partial h_{\alpha\beta} / \partial k_\nu) d_{\beta\gamma'}(\mathbf{k})$.²⁴ \hbar and e (> 0) are Planck's constant and electric charge, respectively. In the present numerical calculation, $\sigma_\nu(T)$ and $\sigma_\nu(\epsilon, T)$ are normalized by $\sigma_0 = e^2 / (\pi \hbar)$.

Using $\sigma_\nu^{\gamma\gamma'}(\epsilon, T)$, the Seebeck coefficient S_ν is obtained by

$$S_\nu(T) = \frac{L_{12}^\nu}{T L_{11}^\nu} = \sum_{\gamma, \gamma'} S_\nu^{\gamma\gamma'}(T), \quad (14)$$

where the component is expressed as

$$\begin{aligned} S_\nu^{\gamma\gamma'}(T) &= \frac{1}{T L_{11}^\nu} \times \\ &\frac{-1}{e} \int_{-\infty}^{\infty} d\epsilon \left(-\frac{\partial f(\epsilon - \mu)}{\partial \epsilon} \right) \times (\epsilon - \mu) \sigma_\nu^{\gamma\gamma'}(\epsilon, T). \end{aligned} \quad (15)$$

Note that the diagonal components of $(\gamma, \gamma') = (1, 1)$ and $(2, 2)$ give the intraband contribution and the off-diagonal components give the interband contribution.

To calculate the spectral conductivity of Eq. (13), we need the relaxation rate Γ_γ of electrons in the γ band. As in the previous paper,²³ we assume

$$\Gamma_\gamma = \Gamma + \Gamma_{\text{ph}}^\gamma, \quad (16)$$

where Γ comes from the impurity scattering and $\Gamma_{\text{ph}}^\gamma$ comes from the phonon scattering:

$$\Gamma_{\text{ph}}^\gamma = C_0 R \times T |\xi_{\gamma, \mathbf{k}}|, \quad (17a)$$

$$R = \frac{\lambda}{\lambda_0}, \quad (17b)$$

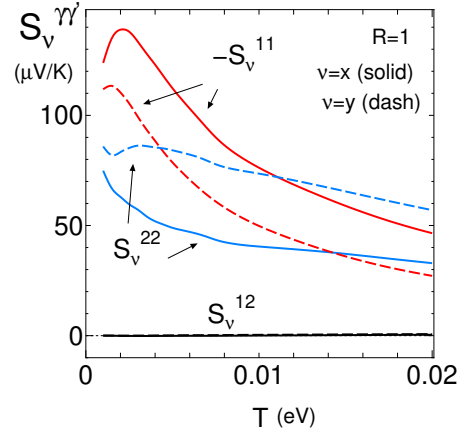


Figure 4. (Color online) T dependence of the components of Seebeck coefficient $S_\nu^{\gamma\gamma'}$ given by Eq. (15). The normalized e-p interaction is taken as $R = 1$, which corresponds to a weak coupling. The solid and dash lines correspond to $\nu = x$ and y , respectively.

where $\lambda = |g_{\mathbf{q}}|^2 / \omega_{\mathbf{q}}$, $\xi_{\gamma, \mathbf{k}} = E_\gamma(\mathbf{k}) - \mu$, $C_0 = 6.25\lambda_0 / (2\pi v^2)$ and $\lambda_0 / 2\pi v = 0.1$. $v \simeq 0.05$ ¹⁴ denotes the averaged velocity of the Dirac cone. λ_0 corresponds to λ for an organic conductor^{57,58} and λ becomes independent of $|\mathbf{q}|$ for small $|\mathbf{q}|$. R is taken as a parameter. We take $\Gamma = 0.0005$ and $R = 1$ mainly in the present numerical calculation.^{23,25}

First, the sign of the Seebeck coefficient is examined by noting that both the conduction and valence bands contribute to the Seebeck coefficient as seen from Eqs. (13), (14) and (15). Since the intraband contribution of Eq. (15) shows $S_\nu^{\gamma\gamma'} < 0$ (> 0) for $\epsilon - \mu > 0$ (< 0), the conduction (valence) band gives the negative (positive) sign for the component of the Seebeck coefficient. Therefore, the sign of the Seebeck coefficient is determined by a competition between the conduction and valence bands. Figure 4 shows the T dependence of $S_\nu^{\gamma\gamma'}$, where the component of $(\gamma, \gamma') = (1, 1)$ is negative due to the conduction band (i.e., electrons) and that of $(2, 2)$ is positive due to the valence band (i.e., holes). The case of $\nu = y$ shows $S_y^{22} < -S_y^{11}$ for $T < 0.004$ and $S_y^{22} > -S_y^{11}$ for $T > 0.004$, respectively. For the y direction, a crossover of the dominant contribution occurs from the electron to the hole with increasing T , while the dominant contribution in the case of $\nu = x$ is always the electron, i.e., $S_x^{22} < -S_x^{11}$ for $T < 0.02$. The interband contribution $S_\nu^{12} (= S_\nu^{21})$ is much smaller than those of the intraband contribution.

Next, we examine the T dependence of the Seebeck coefficients S_x and S_y of Eq. (14). Figure 5 shows S_ν , where solid line, 2-dot dash line and dash line correspond to $R = 1, 0.5$ and 0 , respectively. These lines are calculated for transfer energies with both $\text{Re } w_h$ and $\text{Im } w_h$ in Table I, while the dot line is calculated for transfer energies with only $\text{Re } w_h$. It turns out that $S_y > S_x$ at any temperature. Noticeable behaviors is as follows.

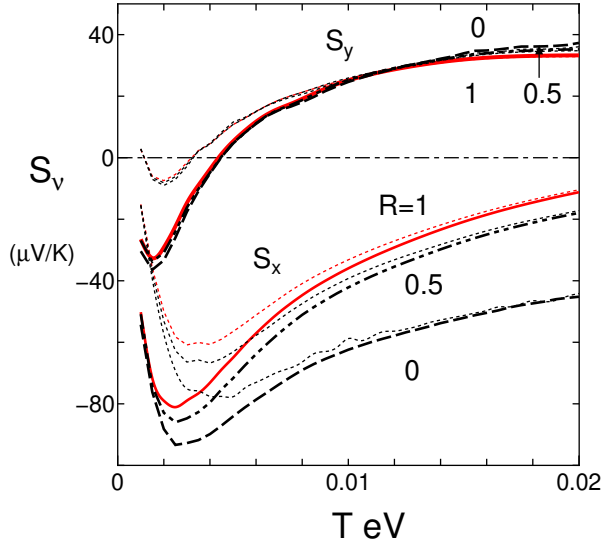


Figure 5. (Color online) T dependence of the Seebeck coefficients S_x and S_y , which is calculated using Eqs. (14) and (15) for $R = 1$ (solid line), $R=0.5$ (2-dot dash line) and $R=0$ (dash line). The chemical potential μ is estimated from the inset of Fig. 2. S_y exhibits a sign change, while $S_x < 0$ for $T < 0.02$. The dot line is obtained for transfer energy with only $\text{Re } w_h$, respectively.

(i) At low temperatures, both $S_y (< 0)$ and $S_x (< 0)$ decrease from zero and take a minimum. With increasing T further, both S_y and S_x start increasing and become close to the respective dot lines.

(ii) At high temperatures, S_y shows a sign change with increasing T . For $R = 1$, S_y undergoes a sign change at $T \simeq 0.004$, where $S_y < 0$ for $T < 0.004$ and $S_y > 0$ for $T > 0.004$. Such a result of $S_y > 0$ at high temperatures is also seen from Fig. 4, where $S_y^{22}(T) > -S_y^{11}(T)$ for $T > 0.004$. The difference in $S_y(T)$ between $R = 1$ and 0 is negligibly small, where $R=1$ denotes the weak e-p coupling and $R=0$ corresponds to the absence of the e-p coupling. Thus, the T dependence for $R = 1$ is determined by the Fermi distribution function, $f(\epsilon - \mu)$, and the effect of the e-p interaction on S_y is negligibly small. On the other hand, there is no sign change for S_x , where $S_x < 0$ in the region of $T < 0.02$. Further, the decrease of R gives the noticeable reduction of $S_x(T)$. The case of $R = 0.5$ suggests the continuous variation of S_ν with decreasing R .

(iii) The role of the SOC is discussed. The solid, 2-dot dash and dash lines are obtained for the transfer energy with both $\text{Re } w_h$ and $\text{Im } w_h$, while dot lines are obtained for transfer energy with only $\text{Re } w_h$. Noting the former lines are slightly lower than the latter line, we can see the SOC enhances the absolute value of the Seebeck coefficient (for $S_\nu < 0$). Such an effect of the SOC becomes large at low temperatures.

In the following we discuss only the case with $R = 1$ that includes the e-p interaction, because both $L_{11}^x(T)$ and $L_{11}^y(T)$ with $R = 0$ increase monotonously with in-

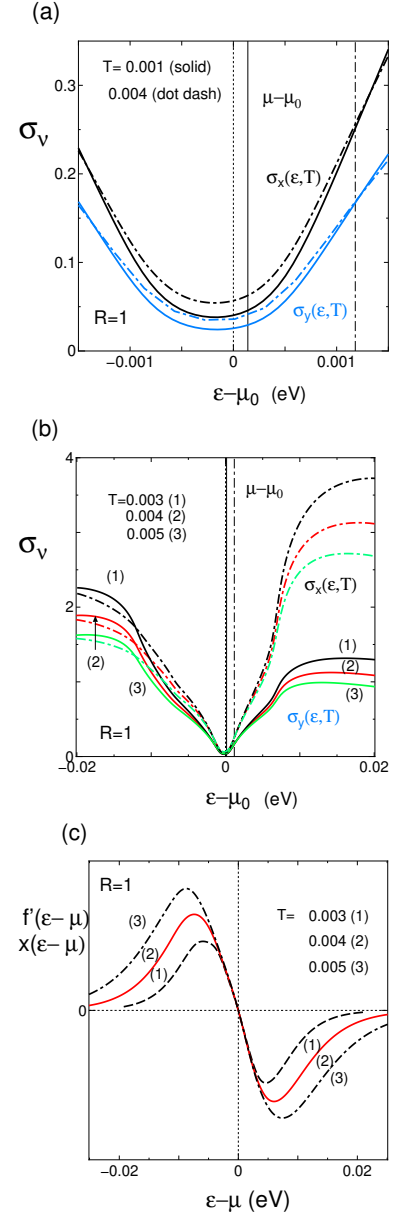


Figure 6. (Color online) (a) Spectral conductivity $\sigma_\nu(\epsilon, T)$ ($\nu = x$ and y) as a function of $\epsilon - \mu_0 (= \tilde{\epsilon})$ with $|\tilde{\epsilon}| < 0.0015$ for $T = 0.001$ and 0.004 . (b) Spectral conductivity $\sigma_y(\epsilon, T)$ (solid line) and $\sigma_x(\epsilon, T)$ (dot dash line) as a function of $\epsilon - \mu_0 (= \tilde{\epsilon})$ with $|\tilde{\epsilon}| < 0.02$ for $T = 0.003$ (1), 0.004 (2) and 0.005 (3). There is the following asymmetry with respect to $\tilde{\epsilon}$. By taking $\tilde{\epsilon} > 0$, one finds $\sigma_x(\tilde{\epsilon} + \mu_0, T) \gg \sigma_y(\tilde{\epsilon} + \mu_0, T)$ and $\sigma_x(\tilde{\epsilon} + \mu_0, T) > \sigma_x(-\tilde{\epsilon} + \mu_0, T) \simeq \sigma_y(-\tilde{\epsilon} + \mu_0, T) > \sigma_y(\tilde{\epsilon} + \mu_0, T)$. (c) $\epsilon - \mu$ dependence of $\partial f(\epsilon - \mu)/\partial \epsilon \times (\epsilon - \mu)$ for the fixed $T = 0.003$ (1), 0.004 (2), and 0.005 (3) corresponding to (b).

creasing T ,³⁴ which is incompatible with that of the experiment.²⁶

IV. ANALYSIS OF THE SEEBECK COEFFICIENTS

To understand the characteristic behavior of the Seebeck coefficient in Fig. 5 that is different from the Seebeck coefficient in α -(BEDT-TTF)₂I₃, we study the spectral conductivity. Noting the main contribution among components of Seebeck coefficient in Fig. 4, is given by intra-band process (i.e., $\gamma = \gamma'$), we rewrite $v_{\gamma\nu}(\mathbf{k}) \equiv v_{\gamma\gamma}^\nu(\mathbf{k})$ and the spectral conductivity, $\sigma_\nu(\epsilon, T)$, as

$$\sigma_\nu(\epsilon, T) = \frac{e^2}{\pi\hbar} \sum_{\gamma=1}^2 \frac{1}{N} \sum_{\mathbf{k}} \sigma_{\gamma\nu}(\mathbf{k}, \epsilon, T), \quad (18)$$

where

$$\sigma_{\gamma\nu}(\mathbf{k}, \epsilon, T) = v_{\gamma\nu}(\mathbf{k})^2 \left(\frac{\Gamma_\gamma}{(\epsilon - E_\gamma(\mathbf{k}))^2 + \Gamma_\gamma^2} \right)^2. \quad (19)$$

The T dependence of the spectral conductivity $\sigma_\nu(\epsilon, T)$ comes from $\Gamma_{\text{ph}}^\gamma$ of Eq. (17a) and $\Gamma_\gamma = \Gamma + \Gamma_{\text{ph}}^\gamma$. Note a special case, where the conduction and valence bands have a symmetry given by $E_1(\mathbf{k}_1) - \mu_0 = -(E_2(\mathbf{k}_2) - \mu_0)$ and $v_{1\nu}(\mathbf{k}_1) = v_{2\nu}(\mathbf{k}_2)$ with $\mathbf{k}_1 - \mathbf{k}_D = -\mathbf{k}_2 + \mathbf{k}_D$. In such a symmetric case, one obtains $\sigma_\nu(\tilde{\epsilon} + \mu_0, T) = \sigma_\nu(-\tilde{\epsilon} + \mu_0, T)$ with $\tilde{\epsilon} = \epsilon - \mu_0$ leading to $L_{12}^\nu = 0$ from Eq. (11). Although such a symmetry is found in a Dirac cone with a linear spectrum, the present model has the band asymmetry, which results in $\sigma_\nu(\tilde{\epsilon} + \mu_0, T) \neq \sigma_\nu(-\tilde{\epsilon} + \mu_0, T)$ and the deviation of the minimum of $\sigma_\nu(\epsilon, T)$ from $\epsilon = \mu_0$.

First, we examine $S_\nu(T)$ at low temperatures, where $S_x < 0$ and $S_y < 0$ in Fig. 5, which is in sharp contrast with those in α -(BEDT-TTF)₂I₃ that show $S_x > 0$ and $S_y > 0$. Figure 6(a) shows the spectral conductivity of $\sigma_x(\epsilon, T)$ and $\sigma_y(\epsilon, T)$ for small $|\epsilon - \mu_0|$ with the fixed $T = 0.001$ and 0.004 . They show a common feature that a minimum of $\sigma_\nu(\epsilon, T)$ ($\nu = x$ and y) is located at ϵ being slightly lower than μ_0 , which is ascribed to the deviation from the linear band around the Dirac point. An inequality of $\sigma_x(\epsilon, T) > \sigma_y(\epsilon, T)$ is consistent with $v_x > v_y$ as discussed in Fig. 3(c). As in the case of α -(BEDT-TTF)₂I₃,¹⁰ we discuss the Seebeck coefficient at low temperatures using the Mott formula,⁵⁹ $S_\nu = -(\pi^2/3e)T\sigma'_\nu(\mu, T)/\sigma_\nu(\mu, T)$. As shown in the inset of Fig. 2, $\mu > \mu_0$. Therefore, one finds that $S_\nu(T) < 0$ due to $\sigma'_\nu(\mu, T) > 0$ in Fig. 6(a) with $\epsilon = \mu(T)$ (the vertical line). This indicates that the Seebeck coefficient is ‘electron-like’. On the other hand, in α -(BEDT-TTF)₂I₃, $\mu < \mu_0$. As a result, the Seebeck coefficient is ‘hole-like’, or $S_\nu(T) > 0$. Furthermore, the origin of $\mu > \mu_0$ in α -(BETS)₂I₃ is the presence of the shoulder C in the DOS as shown in Fig. 2, which originates from the presence of the peak at Y point just below μ_0 .

Next, we examine $S_\nu(T)$ at higher temperatures, Figure 6(b) shows $\sigma_\nu(\epsilon, T)$ with large $|\epsilon - \mu_0|$, which provides L_{12}^ν at higher temperatures. The important feature in

Fig. 6(b) is that $\sigma_x(\epsilon, T)$ is much larger than $\sigma_y(\epsilon, T)$ for $\epsilon - \mu_0 > 0$. Furthermore, $\sigma_y(\epsilon, T)$ for $\epsilon - \mu_0 > 0$ is smaller than $\sigma_y(\epsilon, T)$ for $\epsilon - \mu_0 < 0$. The shoulder near $\epsilon - \mu_0 = 0.007$ corresponds to the energy of the van Hove singularity at A in Fig. 2. We consider that these features in $\sigma_\nu(\epsilon, T)$ is the physical origin of the sign change of S_y , as discussed below.

As seen from Eq. (11), L_{12}^ν is calculated from $\sigma_\nu(\epsilon, T)$ multiplied by

$$\left(\frac{\partial f(\epsilon - \mu)}{\partial \epsilon} \right) (\epsilon - \mu), \quad (20)$$

which is shown in Fig. 6(c) at $T = 0.003$ (1), 0.004 (2), and 0.005 (3). As temperature increases, the peak position of Eq. (20) moves to larger $|\epsilon - \mu|$. As a result, the center of the weight for $\sigma_y(\epsilon, T)$ also moves to larger $|\epsilon - \mu|$. We can see that L_{12}^x is negative for every temperature after integral with respect to ϵ . On the other hand, L_{12}^y changes its sign at $T = 0.004$. Actually, for $T = 0.003$, the electron contribution ($\epsilon - \mu > 0$) is larger than the hole contribution ($\epsilon - \mu < 0$), while for $T = 0.005$, the electron contribution becomes less than the hole contribution.

We examine the difference between $\sigma_y(\epsilon, T)$ and $\sigma_x(\epsilon, T)$ in the region of $\epsilon - \mu_0 > 0.007$ in Fig. 6(b), in terms of the velocity $\mathbf{v}_\gamma(\mathbf{k})$, ($\gamma = 1$ and 2), which is directly related to $\sigma_\nu(\epsilon, T)$ by Eq. (19). Note that the velocity is calculated from

$$\mathbf{v}_\gamma(\mathbf{k}) = (v_{\gamma x}, v_{\gamma y}) = \left(\frac{\partial E_\gamma(\mathbf{k})}{\partial k_x}, \frac{\partial E_\gamma(\mathbf{k})}{\partial k_y} \right). \quad (21)$$

Since \mathbf{v}_γ is perpendicular to the tangent of the contour line of $E_\gamma(\mathbf{k})$, a ratio of $v_{\gamma x}/v_{\gamma y}$ is equal to the slope of the tangent line. At $\epsilon - \mu_0 \sim 0.007$, the dominant contribution comes from the DOS with a van Hove singularity at A in Fig. 2. From Fig. 3(d), the ratio of v_{1y}/v_{1x} near the M' point is given by $\simeq 0.54$ leading to $(v_{1x}/v_{1y})^2 \simeq 3.5$, which is larger than $\sigma_y(\epsilon, T)/\sigma_x(\epsilon, T) \simeq 2.3$ for $\epsilon - \mu_0 \simeq 0.0074$. Such a difference is reduced if the former is averaged on the contour with $E_1 - \mu_0 \simeq 0.0074$ in Fig. 3(d). On the other hand, a fact that $\sigma_y(\epsilon, T) \simeq \sigma_x(\epsilon, T)$ for $\epsilon - \mu_0 \simeq -0.014$ is understood as follows. In this case, the dominant contribution comes from DOS with a van Hove singularity at B in Fig. 2. From Fig. 3(e), the ratio v_{1y}/v_{1x} near the Y point and two saddle points is given by $\simeq 1.0$ leading to $(v_{1x}/v_{1y})^2 \simeq 1.0$, which is almost equal to $\sigma_y(\epsilon, T)/\sigma_x(\epsilon, T) \simeq 1$ for $\epsilon - \mu_0 \simeq -0.014$.

We conclude the present calculation as follows. The results $S_y > 0$ and $S_x < 0$ in α -(BETS)₂I₃ at high temperatures are understood from the anisotropy of the spectral conductivity, $\sigma_\nu(\epsilon, T)$ with respect to ϵ , which comes from the difference in the ratio of v_x/v_y between the conduction and valence bands. The conduction band gives $|v_x/v_y| \gg 1$ due to a large inclination of the line connecting the two Dirac points and the M' point of TRIM, while the valence band gives $|v_x/v_y| \simeq 1$ due to a moderate inclination with $\simeq 1$ of a line connecting the two Dirac points, two saddle points, and the Y point of TRIM.

V. SUMMARY AND DISCUSSION

We have examined the T dependence of the Seebeck coefficient for the Dirac electrons in α -(BETS) $_2$ I $_3$ at ambient pressure using a TB model obtained from the first-principles DFT calculation. Summary and discussion are as follows.

At low temperatures, the sign of the Seebeck coefficient is negative in both x and y directions, i.e., $S_x < 0$ and $S_y < 0$, indicating the electron behavior. The sign of the Seebeck coefficient is determined not only by the sign of $\mu - \mu_0$ but also by the velocities $v_{\gamma\nu}(\mathbf{k})$ of the conduction and valence bands. Thus, we calculated the spectral conductivity, $\sigma_\nu(\epsilon, T)$ at low temperatures to find that the energy derivative of $\sigma_\nu(\epsilon, T)$ with respect to ϵ at $\epsilon = \mu$ takes a positive sign leading to $S_\nu < 0$. This comes from the fact that the chemical potential $\mu(T)$ becomes larger than μ_0 because of the presence of the shoulder just below μ_0 in DOS (i.e., energy maximum at Y point.) This is in sharp contrast to the case of α -(BEDT-TTF) $_2$ I $_3$, in which $\mu(T)$ becomes smaller than μ_0 .

At high temperatures, we obtain $S_y > 0$ and $S_x < 0$, where S_y undergoes the sign change. Such a difference is understood from the spectral conductivity with the large $|\epsilon - \mu|$ showing that $\sigma_y(\epsilon, T)$ with $\epsilon > \mu$ is much smaller than $\sigma_y(\epsilon, T)$ with $\epsilon < \mu$. Furthermore, S_ν was analyzed in terms of the spectral conductivity and the factor $\left(\frac{\partial f}{\partial \epsilon}\right)(\epsilon - \mu)$. $S_y = 0$ at $T=0.004$ is interpreted as the contribution from the valence band becomes equal to that of the conduction band, while, for S_x , the contribution from the valence band is always smaller than that of the conduction band. The present result is obtained for the weak e-p coupling ($R \sim 1$), which is a reasonable choice to reproduce the conductivity at high temperatures³⁴ in the organic conductor.

Finally, our present work on BETS is compared with that by Ohki *et al.* [Phys. Rev B **102**, 235116 (2020)].³⁵ They examined the electronic states at low temperatures, where the transfer energies are derived in the absence of the SOI and the SOI is taken into account as a tunable parameter. The on-site repulsive interaction is introduced to examine the spin ordered state. In the present work, we examined the electronic state mainly at high temperatures, where the on-site repulsive interaction is discarded due to the normal state. In terms of the full-relativistic treatment of the first-principles density functional calculation, the SOC is obtained without adjustable parameters. Further, the e-p scattering is taken into account, which increases with temperature.

ACKNOWLEDGMENTS

We thank T. Furukawa and N. Nishikawa (Tohoku University) for useful discussions and sending us with data of the Seebeck coefficient of BETS. One of the authors (Y.S.) is indebted to H. Fukuyama for valuable com-

ments on the spectral conductivity. This work was supported by a Grant-in-Aid for Scientific Research (Grants No.JP23H01118 and JP23K03274) and JST-Mirai Program Grant Number JPMJMI19A1.

Appendix A: Matrix Elements in the TB Model

Using first-principles calculations, the TB model is obtained as³²

$$\begin{aligned} H_0 &= \sum_{i,j=1}^N \sum_{\alpha,\beta} \sum_{s,s'=\pm} t_{ij;\alpha s,\beta s'} a_{i\alpha s}^\dagger a_{j\beta s'} \\ &= \sum_{\mathbf{k}} \sum_{s,s'} \sum_{\alpha,\beta} h_{\alpha\beta;s s'}(\mathbf{k}) a_{\alpha s}^\dagger(\mathbf{k}) a_{\beta s'}(\mathbf{k}). \end{aligned} \quad (\text{A1})$$

We introduce site-potentials acting on B and C sites, ΔV_B and ΔV_C , which are measured from site-energy at A (A') site, V_A .

$$\Delta V_B = V_B - V_A, \quad (\text{A2})$$

$$\Delta V_C = V_C - V_A, \quad (\text{A3})$$

where V_A , V_B , and V_C are the site-energies at each molecule that are calculated using MLWFs $|\phi_{\alpha,0}\rangle$;

$$V_\alpha = \langle \phi_{\alpha,\sigma,0} | H | \phi_{\alpha,\sigma',0} \rangle, \quad (\text{A4})$$

where $\alpha = A$ ($= A'$), B , and C . molecules. These transfer energies are listed in Table I, where ΔV_C is modified from 0.0208 due to a correlation effect.³²

Since the case of SOC only with the same spin is examined, we rewrite Eq. (A1) as (discarding spin)

$$H_0 = \sum_{\mathbf{k}} \sum_{m=1}^4 \sum_{n=1}^4 h_{mn}(\mathbf{k}) a_m^\dagger(\mathbf{k}) a_n(\mathbf{k}), \quad (\text{A5})$$

where $a_{\alpha s}$ is replaced by a_m and $m, n = 1, 2, 3$, and 4 correspond to A , A' , B and C , respectively.

Using transfer energies given by Table I, a matrix element $h_{mn}(\mathbf{k})$ is calculated from Eq. (4b), where nearest neighbor and next-nearest neighbor sites (Fig. 1) are taken into account.³² The y axis is taken as the negative direction to give the result being consistent with the previous case.^{32,34}

In terms of $X = e^{ik_x}$, $\bar{X} = e^{-ik_x}$, $Y = e^{ik_y}$, and $\bar{Y} = e^{-ik_y}$, matrix elements, h_{mn} , are given by

$$\begin{aligned} h_{11} &= h_{22} = a_{1d}(Y + \bar{Y}) + s1^* X + s1 \bar{X}, \\ h_{33} &= a_{3d}(Y + \bar{Y}) + s3(X + \bar{X}) + \Delta V_B, \\ h_{44} &= a_{4d}(Y + \bar{Y}) + s4(X + \bar{X}) + \Delta V_C, \\ h_{12} &= a_3 + a_2 Y + d_0 \bar{X} + d_1 X Y, \\ h_{13} &= b_3 + b_2 \bar{X} + c_2 \bar{X} Y + c_4 \bar{X} \bar{Y}, \\ h_{14} &= b_4 Y + b_1 \bar{X} Y + c_1 \bar{X} + c_3, \\ h_{23} &= b_2 + b_3 \bar{X} + c_2 \bar{Y} + c_4 Y, \\ h_{24} &= b_1 + b_4 \bar{X} + c_1 Y + c_3 \bar{X} Y, \\ h_{34} &= a_1 + a_1 Y + d_2 \bar{X} + d_3 X + d_2 X Y + d_3 \bar{X} Y, \end{aligned} \quad (\text{A6})$$

and $h_{ji} = h_{ij}^*$.

* suzumura.yoshikazu.k7@a.mail.nagoya-u.ac.jp

† tsumu@kumamoto-u.ac.jp

‡ ogata@phys.s.u-tokyo.ac.jp

- ¹ K. S. Novoselov, A. K. Geim, S. V. Morozov, D. Jiang, M. I. Katsnelson, I. V. Grigorieva, S. V. Dubonos, and A. A. Firsov, *Nature* **438**, 197 (2005).
- ² K. Kajita, Y. Nishio, N. Tajima, Y. Suzumura, and A. Kobayashi, *J. Phys. Soc. Jpn.* **83**, 072002 (2014).
- ³ T. Mori, A. Kobayashi, Y. Sasaki, H. Kobayashi, G. Saito, and H. Inokuchi, *Chem. Lett.* **13**, 957 (1984).
- ⁴ S. Katayama, A. Kobayashi, and Y. Suzumura, *J. Phys. Soc. Jpn.* **75**, 054705 (2006).
- ⁵ A. Kobayashi, S. Katayama, K. Noguchi, and Y. Suzumura, *J. Phys. Soc. Jpn.* **73**, 3135 (2004).
- ⁶ R. Kondo, S. Kagoshima, and J. Harada, *Rev. Sci. Instrum.* **76**, 093902 (2005).
- ⁷ R. Kondo, S. Kagoshima, N. Tajima, and R. Kato, *J. Phys. Soc. Jpn.* **78**, 114714 (2009).
- ⁸ H. Kino and T. Miyazaki, *J. Phys. Soc. Jpn.* **75**, 034704 (2006).
- ⁹ P. Alemany, J.-P. Pouget, and E. Canadel, *Phys. Rev. B* **85**, 195118 (2012).
- ¹⁰ Y. Suzumura, T. Tsumuraya, and M. Ogata, *J. Phys. Soc. Jpn.* **93**, 054704 (2024).
- ¹¹ Y. Takano, K. Hiraki, Y. Takada, H. M. Yamamoto, and T. Takahashi, *J. Phys. Soc. Jpn.* **79**, 104704 (2010).
- ¹² M. Hirata, K. Ishikawa, K. Miyagawa, M. Tamura, C. Berthier, D. Basko, A. Kobayashi, G. Matsuno, and K. Kanoda, *Nat. Commun.* **7**, 12666 (2016).
- ¹³ N. Tajima, R. Kato, S. Sugawara, Y. Nishio, and K. Kajita, *Phys. Rev. B* **85**, 033401 (2012).
- ¹⁴ S. Katayama, A. Kobayashi, and Y. Suzumura, *Eur. Phys. J. B* **67**, 139 (2009).
- ¹⁵ A. Kobayashi, Y. Suzumura, and H. Fukuyama, *J. Phys. Soc. Jpn.* **77**, 064718 (2008).
- ¹⁶ M. O. Goerbig, J.-N. Fuchs, G. Montambaux, and F. Piechon, *Phys. Rev. B* **78**, 045415 (2008).
- ¹⁷ K. Kajita, T. Ojio, H. Fujii, Y. Nishio, H. Kobayashi, A. Kobayashi, and R. Kato, *J. Phys. Soc. Jpn.* **61**, 23 (1992).
- ¹⁸ N. Tajima, M. Tamura, Y. Nishio, K. Kajita, and Y. Iye, *J. Phys. Soc. Jpn.* **69**, 543 (2000).
- ¹⁹ N. Tajima, A. Ebina-Tajima, M. Tamura, Y. Nishio, and K. Kajita, *J. Phys. Soc. Jpn.* **71**, 1832 (2002).
- ²⁰ N. Tajima, S. Sugawara, M. Tamura, R. Kato, Y. Nishio, and K. Kajita, *Europhys. Lett.* **80**, 47002 (2007).
- ²¹ D. Liu, K. Ishikawa, R. Takehara, K. Miyagawa, M. Tanuma, and K. Kanoda, *Phys. Rev. Lett.* **116**, 226401 (2016).
- ²² N. M. R. Peres, F. Guinea, and A. H. Castro Neto, *Phys. Rev. B* **73**, 125411 (2006).
- ²³ Y. Suzumura and M. Ogata, *Phys. Rev. B* **98**, 161205(R) (2018).
- ²⁴ S. Katayama, A. Kobayashi, and Y. Suzumura, *J. Phys. Soc. Jpn.* **75**, 023708 (2006).
- ²⁵ Y. Suzumura, and M. Ogata, *J. Phys. Soc. Jpn.* **90**, 044709 (2021).
- ²⁶ M. Inokuchi, H. Tajima, A. Kobayashi, T. Ohta, H. Kuroda, R. Kato, T. Naito, H. Kobayashi, *Bull. Chem. Soc. Jpn.* **68**, 547 (1995).
- ²⁷ T. Takahashi, Y. Nogami and K. Yakushi, *J. Phys. Soc. Jpn.* **75**, 051008 (2006).
- ²⁸ K. Hiraki, S. Harada, K. Arai, Y. Takano, and T. Takahashi, *J. Phys. Soc. Jpn.* **80**, 01475 (2011).
- ²⁹ S. Kitou, T. Tsumuraya, H. Sawahata, F. Ishii, K. Hiraki, T. Nakamura, N. Katayama, H. Sawa, *Phys. Rev. B*, **103**, 035135 (2021).
- ³⁰ S. M. Winter, K. Riedel, and Valenti, *Phys. Rev. B* **95**, 060404(R) (2017).
- ³¹ T. Osada, *J. Phys. Soc. Jpn.* **87**, 075002 (2018).
- ³² T. Tsumuraya and Y. Suzumura, *Eur. Phys. J. B*, **94**, 17 (2021).
- ³³ M. Ogata, S. Ozaki, and H. Matsuura, *J. Phys. Soc. Jpn.* **91**, 023708 (2022).
- ³⁴ Y. Suzumura and T. Tsumuraya, *J. Phys. Soc. Jpn.* **90**, 124707 (2021).
- ³⁵ D. Ohki, K. Yoshimi, and A. Kobayashi, *Phys. Rev. B* **102**, 235116 (2020).
- ³⁶ S. Fujiyama, H. Maebashi, N. Tajima, T. Tsumuraya, H-B Cui, M. Ogata, and R. Kato, *Phys. Rev. Lett.* **128**, 027201 (2022).
- ³⁷ D. Ohki, K. Yoshimi, and A. Kobayashi, *Phys. Rev. B* **105**, 205123 (2022).
- ³⁸ R. Kubo, *J. Phys. Soc. Jpn.* **12**, 570 (1957).
- ³⁹ J. M. Luttinger, *Phys. Rev.* **135**, A1505 (1964).
- ⁴⁰ M. Ogata and H. Fukuyama, *J. Phys. Soc. Jpn.* **88**, 074703 (2019).
- ⁴¹ H. Fukuyama, *Annu. Rev. Condens. Matter Phys.* **15**, 1-15 (2024).
- ⁴² R. Kitamura, N. Tajima, K. Kajita, R. Reizo, M. Tamura, T. Naito, and Y. Nishio, *JPS Conf. Proc.* **1**, 012097 (2014).
- ⁴³ T. Konoike, M. Sato, K. Uchida, and T. Osada, *J. Phys. Soc. Jpn.* **82**, 073601 (2013).
- ⁴⁴ D. Ohki, Y. Omori, and A. Kobayashi, *Phys. Rev. B* **101**, 245201 (2020).
- ⁴⁵ Y. Suzumura and M. Ogata, *Phys. Rev. B* **107**, 195416 (2023).
- ⁴⁶ T. Nishikawa, T. Furukawa, S. Iguchi, T. Kato, T. Kobayashi, H. Taniguchi and, T. Sasaki, Private communication.
- ⁴⁷ P. Hohenberg, and W. Kohn, *Phys. Rev.* **136**, B864 (1964).
- ⁴⁸ W. Kohn, and L. J. Sham, *Phys. Rev.* **140**, A1133 (1965).
- ⁴⁹ N. Marzari and D. Vanderbilt, *Phys. Rev. B* **56**, 12847 (1997).
- ⁵⁰ I. Souza, N. Marzari, and D. Vanderbilt, *Phys. Rev. B* **65**, 035109 (2001).
- ⁵¹ P. E. Blöchl, *Phys. Rev. B* **50**, 17953 (1994).
- ⁵² Paolo Giannozzi *et al.*, *J. Phys.: Condens. Matter* **21**, 395502 (2009).
- ⁵³ P. Giannozzi *et al.*, *J. Phys.: Condens. Matter* **29**, 465901 (2017).
- ⁵⁴ J. P. Perdew, K. Burke, and M. Ernzerhof, *Phys. Rev. Lett.* **77**, 3865 (1996).
- ⁵⁵ A. Dal Corso, *Comput. Mater. Sci.* **95**, 337 (2014).
- ⁵⁶ N. Troullier, J.L. Martins, *Phys. Rev. B* **43**, 1993 (1991).
- ⁵⁷ M.J. Rice, L. Pietronero, and P. Brüesch, *Solid State Commun.* **21**, 757 (1977).
- ⁵⁸ H. Gutfreund, C. Hartzstein, and M. Weger, *Solid State Commun.* **36**, 647 (1980).

⁵⁹ M. Jonson and G.D. Mahan, Phys. Rev. B **21**, 4223 (1980).